Noninvasive characterization (EPR, µCT, NMR) of 3D PLA electrospun fiber sponges for controlled drug delivery

Johanna Zech[a,1], Michael Mader[b,1], Daniel Gündel[c,2], Hendrik Metz[a], Andreas Odparlik[c], Seema Agarwal[b], Karsten Mäder[a,*], Andreas Greiner[b,*]

[a] Institute of Pharmacy, Martin Luther University Halle-Wittenberg, Wolfgang-Langenbeck-Straße 4, Halle (Saale) 06120, Germany
[b] Macromolecular Chemistry and Bavarian Polymer Institute, University of Bayreuth, Universitätsstraße 30, Bayreuth 95440, Germany
[c] Department of Nuclear Medicine, Martin Luther University Halle-Wittenberg, Ernst-Grube-Straße 40, Halle (Saale) 06120, Germany

A B S T R A C T

Highly porous 3D-scaffolds, made from cut, electrospun PLA fibers, are relatively new and promising systems for controlled drug-delivery applications. Because knowledge concerning fundamental processes of drug delivery from those scaffolds is limited, we noninvasively characterized drug-loading and drug-release mechanisms of these polymer-fiber sponges (PFS). We screened simplified PFS-implantation scenarios with EPR and µCT to quantify and 3D-visualize the absorption of model-biofluids and an oil, a possible drug-loading liquid. Saturation of PFS (6×8 mm, h x d) is governed by the high hydrophobicity of the material and air-entrapment. It required up to 45 weeks for phosphate-buffered saline and 11 weeks for a more physiological, surface-active protein-solution, indicating the slow fluid-uptake of PFS as an effective mechanism to substantially prolong the release of a drug incorporated within the scaffold. Medium-chain triglycerides, as a good wetting liquid, saturated PFS within seconds, suggesting PFS potential to serve as carrier-vessels for immobilizing hydrophobic drug-solutions to define a liquid's 3D-interface. Oil-retention under mechanical stress was therefore investigated. ^{1}H NMR permitted insights into PFS-oil interaction, confirming surface-relaxation and restricted diffusion; both did not influence drug release from oil-loaded PFS. Results facilitate better understanding of PFS and their potential use in drug delivery.

1. Introduction

Controlled release over extended periods of time (days, weeks, months) has important applications in drug therapy for humans and animals, but also in agriculture, environmental sciences, and other areas. For drug therapy in humans, essential applications include the treatment of cancer, local inflammation, infections, schizophrenia or growth-hormone deficiencies. Currently, the dominating material by far is polylactide (PLA) or poly(lactide-*co*-glycolide) PLGA. Dosage forms include mainly preformed implants, microparticles and in-situ forming implants. Current problems of existing delivery systems for controlled release include, but are not limited to, complex manufacturing steps, undesirable release profiles (e.g., high burst release or lag times of

several weeks), the in vivo injection of organic solvents for in-situ forming implants and autocatalytic polymer-degradation leading to faster degradation of larger particles (Siepmann et al., 2005) and very acidic microenvironments (pH around 2 (Mäder et al., 1996; Schädlich et al., 2014)). This acidic microenvironment might also lead to drug degradation prior to release (Guo et al., 2019; Lucke et al., 2002). Consequently, there is a need for the development of new and alternative, controlled-release drug delivery systems. A relatively new and very attractive option is the use of polymer fiber sponges (PFS), highly porous 3D scaffolds made from electrospun polymer fibers.

Electrospinning is a versatile scaffolding tool that reproducibly turns various polymer formulations into a variety of electrospun fibers of adjustable size, size distribution and porosity (Greiner and Wendorff,

2007). Electrospun scaffolds are applied in tissue engineering and have been developed as carriers for prolonged drug release, both intracranially and intraperitoneally (Li et al., 2018; Ranganath and Wang, 2008; Tseng et al., 2015). Their 2D sheet-like shape, however, features a low specific pore volume and demands for large incisions in order to place the implants at the site of treatment.

Freeze-drying is frequently used to produce 3D scaffold sponge systems that are successfully applied for the delivery of different compounds (Duarte et al., 2005; Kassem et al., 2015; Tihan et al., 2015; Zhang et al., 2018). They have been translated into clinical practice as, e.g., the implantable gentamycin-releasing collagen sponge GENTA-COLL® resorb. Fabrication of such sponges is done by lyophilization of polymer solutions. This allows creating drug-loaded scaffolds with micro- and macro-sized matrix patterns of tunable pore structure but strong limitations in the parallel, precise regulation of the pore-wall characteristics. Pore-wall thickness and distribution, as well as the pore-interconnectivity, however, are decisive to adjust drug release, pore-interdiffusion and release from the scaffold.

In this regard, the advantages of ultra-light electrospun PFS are eye-catching (Duan et al., 2015; Si et al., 2014). They synergize the advantages of electrospinning and freeze-drying to create a compact, 3D porous drug-carrier matrix with user-adjustable nano-, micro- and macro-scale dimensions. They can be produced from different materials, including degradable polymers (Mader et al., 2018), and have proven their versatility in various applications, such as extreme temperature and fire insulation (Si et al., 2018), as emulsion separator (Si et al., 2015), catalyst (Duan et al., 2016) and drug carrier (Duan et al., 2017a, 2017b).

The PFS matrix comes with a high fiber-loading capacity which can, through a coating, e.g., chemical vapor deposition (CVD) (Duan et al., 2016) of poly(para xylylene) (PPX) (Simon et al., 1998), be specifically modified to tune the drug release profile (Duan et al., 2017a). By using electrospun fibers instead of polymer solutions in common freeze-drying, the wall-thickness factor is replaced by a controllable fiber diameter. It provides a stable, 3D fiber structure, with an all-directional, open-porous fiber network of adjustable porosity and unlimited pore interconnectivity, both promoting drug accessibility. Direct drug-processing during electrospinning and the narrow fiber-diameter distribution can grant an equal length of drug-diffusion from the fibers in all parts of the scaffold. A. Greiner and coworkers have already used PPX-coated PFS for controlled drug release of an anti-malaria drug (Duan et al., 2017a), (Bagheri et al., 2017), H. Fong and coworkers have introduced a bone growth factor to promote bone formation (Miszuk et al., 2018). It is to be expected that the uptake of body-fluids into these PFS scaffold after implantation could greatly determine drug release and is probably mostly controlled by the wetting of the scaffolds. Hydrophobicity of the material is, therefore, another crucial factor that can be modified by, e.g., coating or plasma treatment (Mader et al., 2018). Due to their large specific pore-volume (up to 99.8%), PFS can also carry huge amounts of medium without collapsing or losing shape. This makes them highly attractive as drug-solution carrier-vessel, as the liquid is forced into a predictable geometrical shape, which is favorable for controlled, equable and prolonged drug release.

The combination of two principles of drug loading, (a) drug incorporation within the fiber scaffold and (b) liquid-loading of the PFS pore-system with drug solutions, can turn them into versatile multi-drug carriers that can flexibly provide user-adjustable doses and drug combinations at the point-of-care (Jennings et al., 2016; Parker et al., 2015). The fundamental processes prevailing inside of PFS, including liquid-uptake/loading and release mechanisms from the scaffold, are still hardly understood. It was, therefore the aim of this study to investigate these processes in more detail and noninvasively, utilizing μCT, NMR measurements, EPR spectroscopy and EPR Imaging. EPR spectroscopy and EPR imaging can provide valuable information on drug delivery processes, including micro-viscosity, micro-polarity, micro-pH and oxygen content (Lurie and Mäder, 2005; Mäder et al.,

1997; Schreier et al., 2014). Spectral-spatial imaging permits to assign the spectra to a specific layer of a sample (Yu et al., 2019). Thus liquid-progression in the PFS is traced and visualized by EPR imaging and confirmed by 3D μCT images of the samples. The influence of hydrophobicity, as well as residual air inside the scaffolds, on fluid-penetration is evaluated. In addition, basic structural integrity, reversible elasticity and different liquid-retention scenarios under compression stress situations are studied, applying standardized mechanical force on empty and liquid-filled PFS over a number of different testing cycles.

The liquid-PFS interaction is investigated for medium-chained triglycerides (MCT) via ^{1}H NMR, quantifying diffusion coefficients and transverse T_2/spin-spin-relaxation times. Both parameters give insight into whether oil molecules experience strong interaction with the PFS material. Changes in the diffusion coefficient would point to restricted diffusion, due to oil-fiber interaction or small pore size of the matrix. Similarly, alterations of T_2 for immobilized oil could suggest surface-relaxation of liquid molecules at the oil-fiber interface, facilitated by oil-scaffold interaction. As such interactions could influence the release profile of a model-drug, a comparative in-vitro drug release study of oil-loaded PFS versus free oil is performed. The release of the paramagnetic compound is followed semi-quantitatively with standard EPR.

The overall results will lead to a better understanding of controlled drug delivery processes and mechanisms from 3D electrospun polymer fiber sponges, which will enable rational design and optimization of such systems.

2. Materials and methods

2.1. Materials

Polylactide (Ingeo Biopolymer PLA 4043D, Nature-Works LLC, USA) (PLA) and [2.2]para-cyclo-phane (PPX–C, SCS coatings, USA, Lot.: 17A20009) (PPX) are used as received. The paramagnetic EPR spin probe 4-Hydroxy-Tempo-d17 (4-Hydroxy-2,2,6,6-tetra-methyl-piper-idine-d17–1–oxyl) (dTempol) is manufactured by ISOTEC®, Merck KGaA, Germany (Table 1), 3-Carbamoyl-proxyl 15 N-nitroxide 3-Car-bamoyl-2,2,5,5,-tetra¬methyl-3-pyrrolidin-1-oxyl (^{15}N-PCM) by Merck / Millipore Sigma, USA. Bovine serum albumin, fraction V (> 98%, low endotoxin, CELLPURE®, Mw ~ 66,000 g/mol) (BSA) is purchased from Carl Roth GmbH + Co. KG, Germany. Miglyol ® 812 (Caprylic /Capric Triglycerides / medium-chained triglycerides Ph. Eur.) (MCT) is obtained from Sasol Olefins & Surfactants GmbH, Germany. All other chemicals are of analytical grade. Double distilled water is used in all experiments.

2.2. Fabrication of samples

The PFS were prepared from electrospun PLA-fiber nonwovens, as published recently (Mader et al., 2018). The cylindrical-shaped PFS were cut in frozen medium to achieve highly comparable PFS with narrow density (12.5 ± 1.0) mg/cm^3, shape- and size distribution (Height h: (6.1 ± 0.1) mm and Diameter d: (8.0 ± 0.04) mm). The PFS were subsequently coated with PPX prior to use, reaching a final density of (28 ± 1.5) mg/cm^3. The PFS oil-loading capacity was determined as drained net weight after slowly immersing the PFS in MCT and subsequent gravimetric analysis.
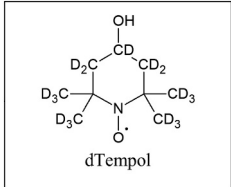
2.3. PPX-coating with thickness and hydrophilicity analysis

The PLA PFS were coated with PPX by CVD and characterized as previously reported (Duan et al., 2016). Six PLA PFS were fastened to a cannula tip and placed inside the reaction chamber (Labcoater 1, SCS Germany GmbH), together with an ethanol-cleaned glass slide for indirect coating thickness evaluation, using a Dektak profilometer (Surface Profiler 150, Veeco Instruments Inc.). PFS depth-dependent SEM PPX coating-thickness evaluations were performed using ImageJ.

Table 1
Pharmaceutically relevant model-liquids and the chemical structure of the EPR spin probe 4-Hydroxy-Tempo-d$_{17}$ (dTempol) used to study the uptake of different fluids into the PFS and model drug release studies.

Liquid system	Model	Liquid*
PBS	Aqueous/hydrophilic	Phosphate-buffered saline pH 7.4 Ph. Eur preserved with 0.02% NaN$_3$
5% BSA	Surface-active protein-solution model for bodily fluid	5.0 wt% Bovine serum albumin in PBS
MCT	Hydrophobic oil, suitable for drug loading of PFS	Medium-chained triglycerides *Miglyol 812®*

dTempol

*1 mM dTempol is added for EPR measurements.

Indirect coating-thickness evaluations were carried out by placing a control glass-slide near the PFS during the coating process to achieve a general thickness of about 1 μm for all PPX-coated samples. As this technique cannot represent the coating thickness throughout the whole PFS scaffold, detailed coating thickness gradient evaluations using SEM imaging were performed, by subtraction of the mean coated- and the non-coated-fiber diameter. As expected, the received coating thickness achieved with static CVD is decreasing with reaching deeper PFS areas (Fig. S1). Beyond 300 μm, along the way inside towards the PFS core, the coating thickness is slowly, asymptotically decreasing from 1.2 μm to about 400 nm within 500 μm of scaffold-depth.

The hydrophobicity was measured by contact angle measurements. The water contact angle of PFS was measured on a Drop Shape Analyzer (Krüss Advance, v1.3.1) using Milli-Q water as a 4 μl water droplet. Examples are shown in Fig. S1 bottom.

2.3.1. Scanning electron microscopy

SEM images were recorded on a Zeiss LEO 1530 (FE-SEM, Schottky-field-emission cathode; in-lens and SE 2 detector) at the Bavarian Polymer Institute (BPI, KeyLab Electron and Optical Microscopy) in Bayreuth. An accelerating voltage of 2 kV was used. The samples were sputtered with platinum (1.3 nm) prior to SEM imaging, using a sputter coater (Cressington HR208) with a thickness controller (Cressington MTM20).

2.4. Liquid uptake visualization via EPR Imaging and μCT

To study the uptake rate and mechanism of fluids penetrating the PFS, the PFS samples were incubated with different pharmaceutically relevant model liquids (Table 1).

The PFS were carefully placed in sample holders that were custom-made to fit the PFS size exactly. This allowed penetration of liquid only in one dimension - from the top of the cylinder-shaped PFS - while preventing any leakage of fluids along the sides of the material. The PFS were submersed in the model liquid, tightly sealed and incubated at 37 °C. Fluid levels of 5 mm above the PFS surfaces were maintained at all times to guarantee a constant hydrostatic pressure. During measurements, the PFS remained in the sample holders and were not removed until the end of the experiment. Experiments were done in triplicates, for two types of sample holders, either allowing or preventing the escape of air from the PFS with invading solvent front (closed/open bottom, Table 2).

The liquid uptake over time was monitored with EPR spectroscopy and EPR imaging as well as μCT imaging for PBS and 5% BSA, while MCT uptake is only visualized using μCT scans. Sample holders for EPR and NMR experiments were made from Teflon; a low-density plastic was used for the fabrication of μCT sample holders.

2.4.1. EPR studies

In electron paramagnetic resonance spectroscopy, the amplitude of the signal of the paramagnetic spin probe was used to determine the amount of dTempol taken up by the PFS with PBS or 5% BSA over time. 1D spatial-spectral EPR imaging was applied to visualize the distribution of the spin probe in the samples along the y-axis (**Fig. S5**). EPR measurements were performed using an L-band EPR spectrometer (MagnetTech, Germany), equipped with an additional magnet for variable gradient fixed-orientation imaging. A glass capillary containing a 1 mM solution of 3-Carbamoyl-proxyl ^{15}N-nitroxide 3-Carbamoyl-2,2,5,5-tetramethyl-3-pyrrolidin-1-oxyl (^{15}N-PCM) in methanol / H$_2$O served as internal standard to correct the varying attenuation of the signal due to the changing presence of H$_2$O in the samples. The data was recorded with the Cu3 v.6.1 program (MagnetTech, Germany) and transformed to render spectral-spatial EPR plots. Parameters used for measurements are given in Table S1.

2.4.2. μCT-scans

Micro-computed tomography scans were performed to record 3D images of the distribution of liquid and air in the PFS, allowing to further investigation of the pattern of penetration of the different testing-fluids. X-ray μCT scans were carried out with a NanoScan PET/CT (Mediso, Hungary), in semi-circular mode with one rotation. Reconstruction of the images was done with Nucline Software (Mediso, Hungary), using a Butterworth filter and a voxel size of 125 × 125 × 125 μm, and analyzed with PMOD software (PMOD Technologies, Switzerland). Units in all μCT images are given in Hounsfield units. The following parameters have been used: 720 projections, x-ray energy 70 kVp, exposition time 300 ms, bin 1:4.

Measurements of scaffold-MCT interactions. Small amounts of MCT, a good PFS wetting liquid, added to the top of the PFS network, spread within the very first PFS layers. Time-dependent MCT visualization inside the PFS, using μCT measurements, reproducibly reveal, that the oil does not move deeper into the scaffold within 24 h (Fig. S2).

Porosity calculation of PFS.

The porosity P of the PFS fabricated is calculated as follows (Duan et al., 2017a):

$$P = \left(1 - \frac{\rho_S}{\rho_{bulk}}\right) \cdot 100 \quad SPV = \frac{P}{\rho S \cdot 10^{-3}}$$

$$L_c = dry\ net\ weight \frac{loaded\ PFS}{unloaded\ PFS}$$

With: ρ_s Density of the PFS [mg/cm^3], ρ_{bulk} Density of the bulk material [g/cm^3], SPV Specific Pore Volume [cm^3/g], L_c Loading capacity of a PFS [g/g].

Table 2
Sample holders used for PFS incubation and liquid-uptake results. Duration of liquid-uptake of different model-fluids in the PPX-coated PFS is given in days unless stated otherwise.

	Closed-bottom sample holder		Open-bottom sample holder			
	EPR	μCT	EPR	μCT		
PBS	168 | 245 | 315	131 | 131 | 204	28 | 28 | 28	–		PFS
5% BSA	77 | 77| 77	63 | 70 | 70	–	–		testing fluid
MCT	–	28 | 42 | 42	–	< 5 | < 5 min		

2.5. Compressibility tests

Stress-strain experiments were performed using a Zwick/Roell Z 2.5 (ZwickRoell GmbH & Co. KG) (load sensor 20 N, compressing speed 5 mm/min, 23 °C) following DIN 53421 for cylindrical samples. The PFS samples were placed on and covered with a 170 μm glass slide during the compression to prevent oil crawling.

PFS liquid loading. For PFS liquid-load capacity calculations, the PFS were entirely filled with liquid by unidirectional immersion. The PFS is taken out of solution, and excess of fluid is removed to calculate the net-weight gravimetrically. The individual PFS used for calculation are depicted in Fig. S3.

2.6. ^{1}H NMR studies

To study transversal relaxation time T_2 and the diffusion coefficient D of the oil, both, by itself as free MCT and when located in the fiber scaffolds, ^{1}H NMR measurements were performed with a low-field benchtop Maran Ultra ^{1}H NMR spectrometer (Oxford Instruments, UK). The PFS were completely saturated with MCT, while free MCT samples were kept in sample holders that contained the same volume of MCT in the same shape as the oil-loaded PFS. The sample temperature was maintained at 37 °C during measurements. The Carr-Purcell-Meiboom-Gill sequence with a relaxation delay of 5 s and a receiver gain of 40 was used to determine T_2. Sixty-four scans were acquired for each measurement, and the data processed with the WinDXP software (Oxford Instruments, UK) to give the T_2 distributions. Molecular diffusion of free MCT and oil in the PFS was analyzed using a pulsed-gradient stimulated-echo sequence (Fig. S6).

2.7. Model-drug release

The immobilization of the oil in the PFS material could potentially slow down the release of small drug molecules from MCT-loaded PFS compared to free MCT. The interaction of MCT with the PFS scaffolds, as well as the restricting effect of the PFS structure on free diffusion, could alter release kinetics for the oil-loaded carriers.

To test this hypothesis, we studied the release of dTempol as a model-drug from both free and immobilized MCT. To ensure that the interface between the oil and the release medium is kept the same in both cases, a release apparatus was built. It consists of a tube that either fits one PFS loaded with 280 μl MCT, or the equal volume of oil, shaped as a cylinder of identical dimensions as the PFS (Fig. 7). The MCT contained 2 mmol/kg dTempol, and the release of the spin probe was followed via X-band EPR measurements.

dTempol release was studied under sink conditions at 37 °C in 35 ml PBS pH 7.4 Ph. Eur., while gently shaking the samples. At each time-point, 50 μl of the release medium were collected in a glass capillary, which was then sealed on both ends and analyzed with a MiniScope MS 200 benchtop X-band EPR spectrometer (MagnetTech, Germany).

Measurement parameters can be found in Table S2.

3. Results and discussion

3.1. PFS sample fabrication

The basic fabrication steps to produce the PFS used in this work are performed as published recently (Mader et al., 2018). To investigate the physical processes occurring in PFS during, e.g., long-term incubation scenarios, possible negative impacts on PFS structure or integrity must be avoided. Therefore, all PFS used for our experiments are coated with a thin-layer of PPX by CVD (Duan et al., 2016) to enhance their mechanical properties while maintaining their pore structure and overall hydrophilicity. PPX-coating also minimizes water absorption of the PLA PFS, reducing the risk of hydrolytic degradation of the PLA fiber network during long incubation periods in aqueous environments. Aiming at the potential use of PFS as multi-component drug carrier systems, as mentioned in the introduction, PFS PPX-coating offers several additional advantages with regard to the extension of possible areas of application (Jiang et al., 2018). It has, however, to be said, that PPX as a non-biodegradable material is only suitable for use and implantation where the PFS could be removed easily after complete drug delivery, or ex-vivo application. Therefore, PPX is to be seen mainly as a well-studied model-polymer in our experiments. The development of coating techniques with other - also biodegradable - materials will allow for an even more versatile fine-tuning of the PFS properties, permitting a wide range of different applications in drug delivery and tissue engineering.

3.2. PPX-coating thickness and hydrophilicity analysis

The PLA PFS PPX-coating allows for a precise and almost non-invasive adjustment of the PFS scaffold properties while maintaining its structural characteristics (Duan et al., 2016). The homogeneity of the PPX-coating influences the PFS mechanical properties and drug release from the fibers (Duan et al., 2016). Hence, the PFS coating and wettability, investigated in detail, are given in Fig. S1. Contact angle and SEM coating-thickness quantification investigations are shown. Quantification of the mean depth-dependent fiber diameter shows a sharp decrease in coating thickness within the very first fiber layers. Starting at the top of the PFS, PPX thickness is asymptotically decreasing from 1.2 μm to about 400 nm within 500 μm of PFS-depth. Contact angle measurements reveal that the hydrophilicity is almost unchanged by PPX-coating, with a difference of 136° (PLA) to 144° (PLA-PPX).

3.3. PFS liquid-uptake model scenarios

Biofluids advancing in the PFS scaffold are indispensable for the potential release of drugs incorporated in the fibers in the case of implantation. Preliminary trials of PFS-liquid interaction investigations performed by μCT imaging (Fig. S2) indicate that for MCT, the liquid

perfusion within the PFS is dominated by capillary forces, which are surpassing gravitation. Hence any migration into the scaffold has to be driven by external forces, e.g., excess of liquid or hydrostatic pressure. These forces were simulated by immersion of the PFS to achieve reproducible PFS liquid-loading results.

We investigated the PFS-liquid interaction using three different model-liquids, as the contact angle already indicates the wetting of the hydrophobic scaffold being a major parameter governing liquid-uptake. EPR and µCT imaging are used to visualize the liquid-penetration process. Two sample holders were used for PFS liquid incubation to simulate individual aspects of typical implantation scenarios of PFS imaginable during in-vivo or in-vitro application (Yu et al., 2019). The holders helped to controllably assess the influence and behavior of the liquid-phase progression and the replacing of the void, i.e., the air present inside a PFS. One holder type provides a closed bottom (Table 2, top left); the other has an open bottom (Table 2, top right). The closed-bottom holder encases the PFS on all but one side; hence, air can only exit through or at the interface of the infiltrating liquid. The open-bottom holder allows air to evade from the PFS through the opening, in the opposite direction to the approaching liquid front. Both scenarios were investigated using three PFS samples, respectively. The overall results of the EPR and µCT PFS liquid-load investigations are summarized in Table 2. The hydrophilicity of a drug-delivery system has a crucial influence on its behavior when placed in a particular environment. Poor wettability with aqueous liquids will decidedly affect the absorption of, e.g., bodily fluids by the PFS after implantation, impacting the resulting drug-release profile and the performance of the PFS material in-vivo. Upon incubation with PBS and 5% BSA, a layer of air on the PFS surface indicated the initial non-wetting of the surface.

3.3.1. Tracing liquid-uptake via EPR and µCT imaging

Closed-bottom sample holder. In the closed-bottom sample holder, fluid-penetration and full saturation by PBS was subject to considerable fluctuations, requiring 168 up to 315 days (24–45 weeks) (Fig. 1A) in the EPR experiments. In EPR 1D-imaging, the liquid-penetration progress was visible as one seemingly evenly traveling solvent-front along the y-axis (see Fig. S5).

µCT analysis revealed that in the plastic sample-holders, the liquid preferably intruded the scaffold along the edges of the holders' cavity, steadily enclosing the air inside the PFS (Fig. 2). In the presence of 5%

BSA, air-encapsulation still occurred, but all PFS wee reproducibly fully saturated in 70 (µCT) - 77 (EPR) days (Fig. 1B, Fig. 2). The surface-active BSA decreased the absorption-time of an aqueous liquid around three-fold by increasing wettability, thereby accelerating potential drug release. Nonetheless, the uptake of the BSA-solution was still considerably slow, making drug delivery mainly imaginable for localized treatment with drugs of a very low EC_{50} and high potency. The uptake of MCT, a good PFS wetting liquid (Fig. S1), was completed after 4–6 weeks. µCT scans displayed a liquid-loading mechanism analogous to the PBS and BSA systems (Fig. 2), including a slowly shrinking air pocket.

The encasement of air, acting as a slowly receding barrier, could deliberately be used as a measure to achieve prolonged drug release. The mechanism is similar to what was proposed by Yohe et al. as "using displacement of air to control delivery rates" (Yohe et al., 2012) for super-hydrophobic 2D electrospun fiber mats. Air encapsulated within the PFS needs to be dissolved in the advancing fluid and diffuse to the PFS surface to evade the scaffold. Air solubility in the liquid, shape and surface area of the air pocket and the diffusion coefficient have, therefore, to be considered. However, such an application is only suitable for a site of implantation where the delicate PFS will be protected from mechanical stress, e.g., intracranially or inside bones, as compression could expel the air and change release rates considerably. Gradual displacement of air might also be exploited for dry PFS employed as extractable drug-loaded cartridges ex-vivo, e.g., in an infusion-chamber system, an advancement to what has been suggested for electrospun fiber mats (Bagheri et al., 2017).

Open-bottom holder. Allowing air to be released during incubation instead of placing a PFS in an enclosed cavity or fully immersing it is simulated by using an open-bottom holder (Fig. 3). The two-directional open cavity permits air to evade from the scaffold and avoid its encapsulation. Thereby liquid-uptake rate is greatly increased. A PFS placed on the interface of MCT is completely saturated within less than 30 s, beyond the limit of µCT and EPR visualization and our sampling setup. In the incubation scenario with the open-bottom holder, MCT penetrates the whole PFS in less than 5 min (Fig. 3A), which is more than 10^4 times faster than in a closed-cavity situation. Under analog conditions, the uptake time of PBS is reproducibly decreased from an average of 243 days to 28 days, respectively (Fig. 3B, day 28 not shown). No indication of encapsulated air could be found in µCT
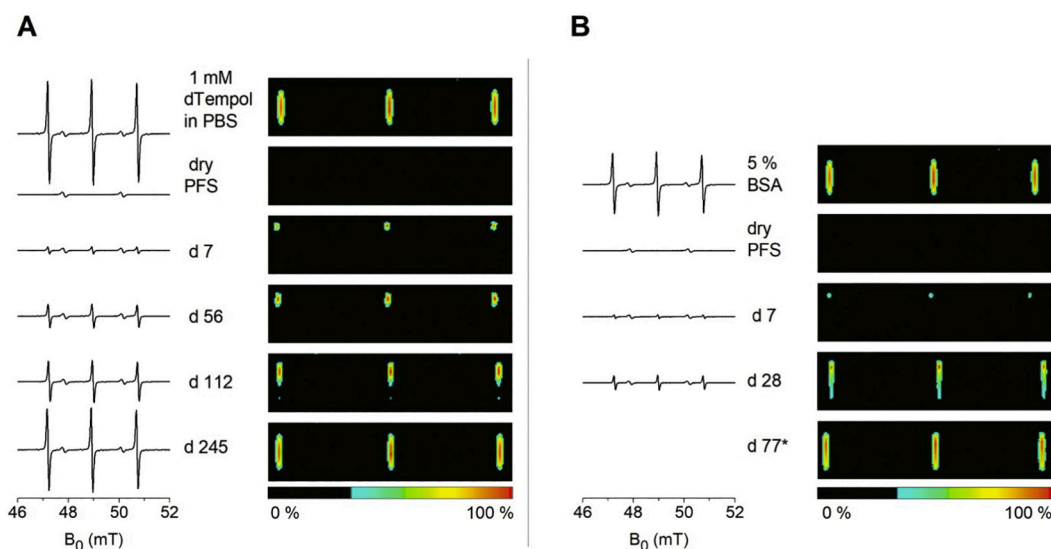

Fig. 1. EPR spectra and the corresponding EPR images of liquid-uptake of PFS incubated in closed-bottom sample holders at 37 °C. The first row shows the signal of the empty sample holder filled with incubation medium. The ^{15}N-PCM reference capillary is accountable for the two signals at 47.8 and 50.2 mT. **A:** PBS pH 7.4 with 1 mM dTempol. **B:** 5% BSA with 1 mM dTempol.
*As the EPR spin probe is slowly degrading in the presence of BSA, reliable semi-quantitative evaluation from EPR spectra is not possible for day 77.
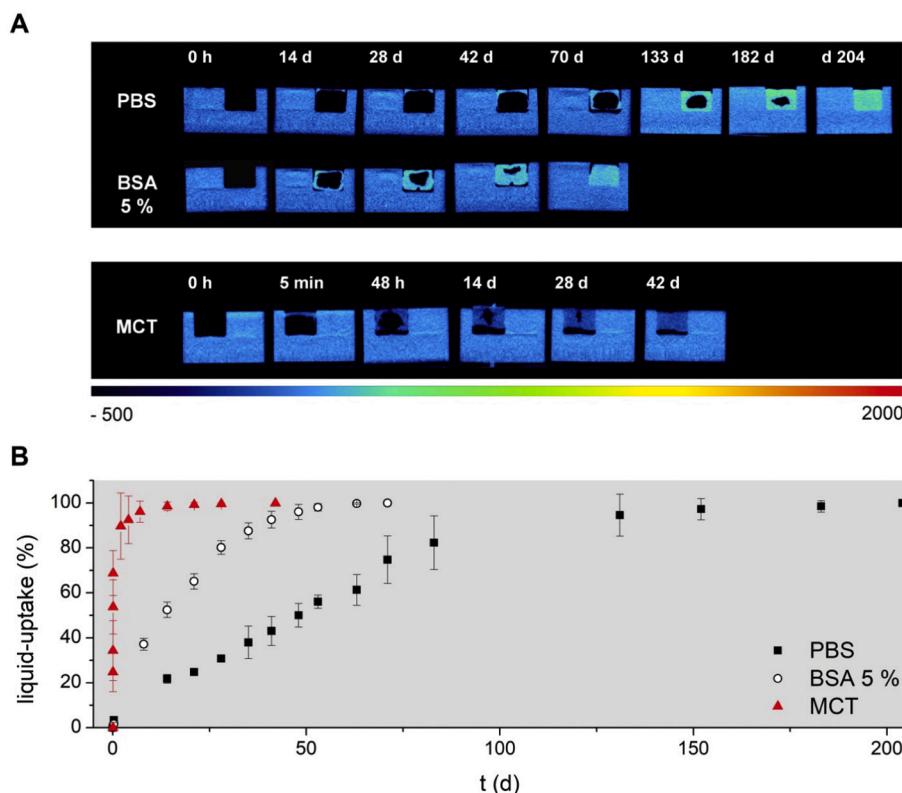
Fig. 2. Liquid-uptake of PFS incubated in closed-bottom sample holder. **A:** µCT scans of one PFS for each of the incubation media. Dry parts of the PFS are not visible due to the low density of the material. **B:** The uptake of liquid for each PFS in volume % of the PFS saturated with fluid.
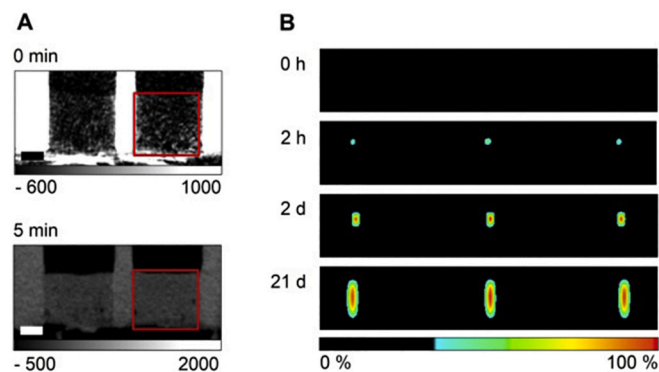

Fig. 3. Liquid-uptake of PFS in open-bottom sample holder, incubated at 37 °C. **A:** µCT scans, top: dry PFS, bottom: PFS completely saturated with MCT after 5 min of incubation (Bar = 3 mm). **B:** EPR images: top: dry PFS, below: PFS incubated with PBS pH 7.4 after 2 h, 2 days and 3 weeks.

measurements.

As neither surface tension nor viscosity alone can reasonably be employed to explain our observations, the penetration of the liquids into the porous PFS system is best described by the Washburn's equation (Washburn, 1921):

$$L = \sqrt{\frac{\gamma r t \cos(\phi)}{2\eta}}$$

L, the depth of fluid penetration over time t is controlled by the surface tension γ and dynamic viscosity η of the fluid, the contact angle ϕ between solid material and tested fluid and the pore radius r. r is considered to be the same for all our samples.

Here, the contact angle, quantifying the interfacial tension at the PFS-liquid interface, is the most influential parameter and best explains

our results. The results further underline that besides the implantation environment (provided exit of air from the samples), wetting of the scaffold is one main parameter governing the liquid uptake in PFS.

3.3.2. Spin probe micro-environment

The EPR spectra acquired in the fluid-uptake experiments also give information on the micro-environment of the spin probe as it enters the pores of the fiber matrix with the incubation medium (Fig. 1), (Kempe et al., 2010; Lurie and Mäder, 2005).

All spectra exhibit hyperfine splitting into three symmetrical, narrow lines of the same amplitude, indicating that the ^{14}N-nitroxide radical dTempol stays mobile, in solution, at all times. No crystallization/immobilization - e.g., as a result of the probe entering the fibers and consequent precipitation - occurred.

Changes in the hyperfine-splitting constant (seen as the distance between lines) over time are not visible, showing that micro-polarity did not change over the course of the experiment. Increasing micro-viscosity would be visible as a broadening of the EPR signals. Such signal variations were not observed here, and we, therefore, conclude that dTempol did not experience any changes to its micro-environment during the incubation of samples. The lack of different environments can be attributed to the high porosity of the system: the entrapped liquid is responsible for the observed EPR signal, no contribution from the solid fibers was observed. The lack of contributions from immobilized spectra results from the low amount of solid material present in the sample and the hydrophilic properties of dTempol. It is noteworthy, that despite the macroscopic immobilization of the liquid in the 3D-matrix, the micro-viscosity and micro-polarity are not changed in comparison to the bulk liquid.

3.4. PFS compression and reversible oil release

If used as drug-solution carrier-vessels, PFS must be able to reliably

Table 3
Overview of all PFS used in this work, their porosity, pore volume in dry and model-liquid loaded state. Corresponding images of representative individual PFS can be found in Fig. S3. The evaluated data of compression experiments shown and performed with dry and loaded PFS.

Material	Density (mg/cm^3)	SPV (cm^3/g)	P (%)	Model liquid	L_c (g/g)	SPV$_{load}$ (%V/V)
PLA	(12.5 ± 1)	79	99	Water	(76 ± 0.4)	(98 ± 0.2)
	(12.5 ± 1)	79	99	MCT	(78 ± 0.2)	(98 ± 0.1)
PLA-c-PPX	(28.0 ± 1.5)	35	98	Water	(35 ± 0.4)	(99 ± 0.2)
	(28.0 ± 1.5)	35	98	MCT	(34 ± 0.3)	(99 ± 0.4)
Compression c500 ε10|20|30	ε_{onset} (%)	Elasticity (%)	Δw (mJ•10^{-2})	σ_{Max} (kPa)	E-Module (kPa)	Oil retention reversible (%)
Dry	2 | 6 | 12	85 | 70 | 60	7 | 3 | 6	7 | 11 | 17	(0.9 ± 0.1)	–
100% load	3 | 6 | 12	70 | 69 | 59	1 | 3 | 4	6 | 9 | 11	(0.7 ± 0.1)	97 | 94 | 88
90% load	5 | - | -	50 | - | -	1 | - | -	3.5 | - | -	0.7 | - | -	100
80% load	- | 13 | -	- | 35 | -	- | 1 | -	- | 5.8 | -	- | 0.8 | -	100
70% load	- | - | 15	- | - | 30	- | - | 3	- | - | 8.4	- | - | 0.6	100

With: SPV Specific Pore Volume; P Porosity; L_c PFS Load capacity; SPV$_{load}$ Filled PFS volume fraction; (see **IS-0**) $\sigma_{Max.}$ Maximum compression stress; ε_{onset} Onset strain, indicating the first measurable stress upon compression, used for elasticity calculation; Elasticity as percentage grade indicating how the system can reversibly return to its original shape after compression at different $\varepsilon_{Max.}$; Δw Compression workload; E-Module; Reversible oil-retention capability of the PFS after the end of compression.

retain loading-fluids, such as oily drug solutions, without changes to the PFS stability and shape. Any unwanted expulsion of drug-solution under mechanical stress that can be reasonably expected during the application of such systems would change the drug-release profile and consequently has to be ruled out.

Uniaxial compression experiments were performed to quantify the impact of PFS oil-loading on the PFS characteristics, including size, shape, elasticity and the oil-retention profile upon pressure. The evaluated and calculated stress-strain, elasticity and oil retention data for all compression experiments after 500 cycles are summarized in Table 3.

3.4.1. PFS compression in dry and fully oil-loaded state

The physical-mechanical properties with and without oil loading and the impact of different oil loads were quantified. Reference measurements were carried out with coated but unloaded, dry PPX PFS. The stress-strain experiments performed were documented by digital photography (Fig. 4). Different maximum compressions ($\varepsilon_{Max.}$) of 10%, 20% and 30% were investigated to quantify the reversibility of the MCT release, and hence, the reabsorption capabilities of PFS.

To assure comparability between the individual PFS compression-experiments performed, the same PFS was used for a complete $\varepsilon_{Max.}$ measuring sequence. A direct comparison between the compression characteristics of a PPX-coated PFS in dry and in a fully loaded state (Fig. 4) is shown. The resulting force-displacement diagrams indicate that there is only a minor loss in the maximum compression. The maximum oil-load capacity as dry net weight is determined gravimetrically for each PFS used before compression. The mean oil-load capacity is found to be in a range of (34 ± 0.3) g MCT per gram of a 6 × 8 mm (h x d) PPX-coated PFS, representing (99 ± 0.4) % of the theoretically available specific pore volume.

Oil was instantaneously released from the fully loaded PFS immediately after starting the compression experiment, as is to be expected. After compression, as the PFS suffers from an $\varepsilon_{Max.}$ dependent height loss, parts of the MCT cannot be reabsorbed by the PFS anymore. This surely is a problem regarding any application because it will make the release from oily drug solutions formerly immobilized in the PFS unpredictable. Therefore, we also investigated PFS loads below the maximum loading-capacity and the resulting impact on the structural behavior of a PFS, its size, elasticity, hence, reversible oil release and reabsorption capabilities.

3.4.2. PFS compression under reduced oil loads

PFS compression at $\varepsilon_{Max.}$ 10% to 30% with different PFS oil-loads, ranging from 70% to 90%, was performed to quantitatively evaluate the

shape integrity of a partially loaded PFS, the MCT release and re-absorption characteristics of coated PFS (Fig. 5) during compression stress. For comprehensibility reasons, it must be said that the negative load value for each PFS is kept equal to the value of $\varepsilon_{Max.}$ applied.

The mechanical results in combination with the images taken of the PFS during measurement reveal that oil always started to leak from PFS at a compression stage of about 70% of the applied $\varepsilon_{Max.}$, independent of PFS load prepared. For clear visualization, timeline images of a PFS loaded with 80% MCT and its gradual compression to 20% $\varepsilon_{Max.}$ are shown in (Fig. S4). The strain at which the oil release is first observed does not seem to vary much within 500 cycles of compression. No air escape from the PFS was noted during compression; hence, no air voids within the PFS seem to have been present or could exit from the inside of the samples. We can, therefore, conclude that each compression within the range of $\varepsilon_{Max.}$ equal to the negative PFS load can assure that the oil is always reabsorbed completely, even after 500 cycles of compression.

3.5. ^{1}H NMR studies

The high oil-loading and -holding capacity of the PFS suggests a strong interaction of MCT with the PFS scaffold at the solid-liquid interface. To better understand these interactions and their impact on drug release, T_2 distributions and diffusion coefficients for free MCT and oil immobilized in the PFS were acquired using ^{1}H NMR.

3.5.1. Transverse magnetization relaxation T_2

Measurements were performed for T_2 in both, free MCT in a cylindrical sample holder, and the same amount of MCT immobilized in PFS of the same dimensions. For free MCT, just one population was found, with T_2 ranging from 100 to 1000 ms (Fig. 6, top left). Only bulk spin-spin relaxation could occur between similar or identical triglycerides, resulting in just one peak.

T_2 distribution of liquids in porous material is influenced by the surface to volume ratio of the material and the consequent surface-relaxation, possible bulk-relaxation, as well as the restricted diffusion in the pores, as laid out in (Kleinberg and Horsfield, 1990). When immobilized in the PFS scaffold, the T_2 relaxation times of MCT were found to represent different populations (Fig. 6, bottom left). The peak at 300 ms can be attributed to the bulk-relaxation of the free MCT in the larger pores of the PFS, while peaks at 1 and 100 ms were not present for free MCT and have to be caused by the effects of the PFS scaffold. Shorter times for T_2 are usually attributed to prolonged interaction between spins due to molecules staying in close proximity to each other. Hence, the presence of the signal at around 1 ms suggests MCT
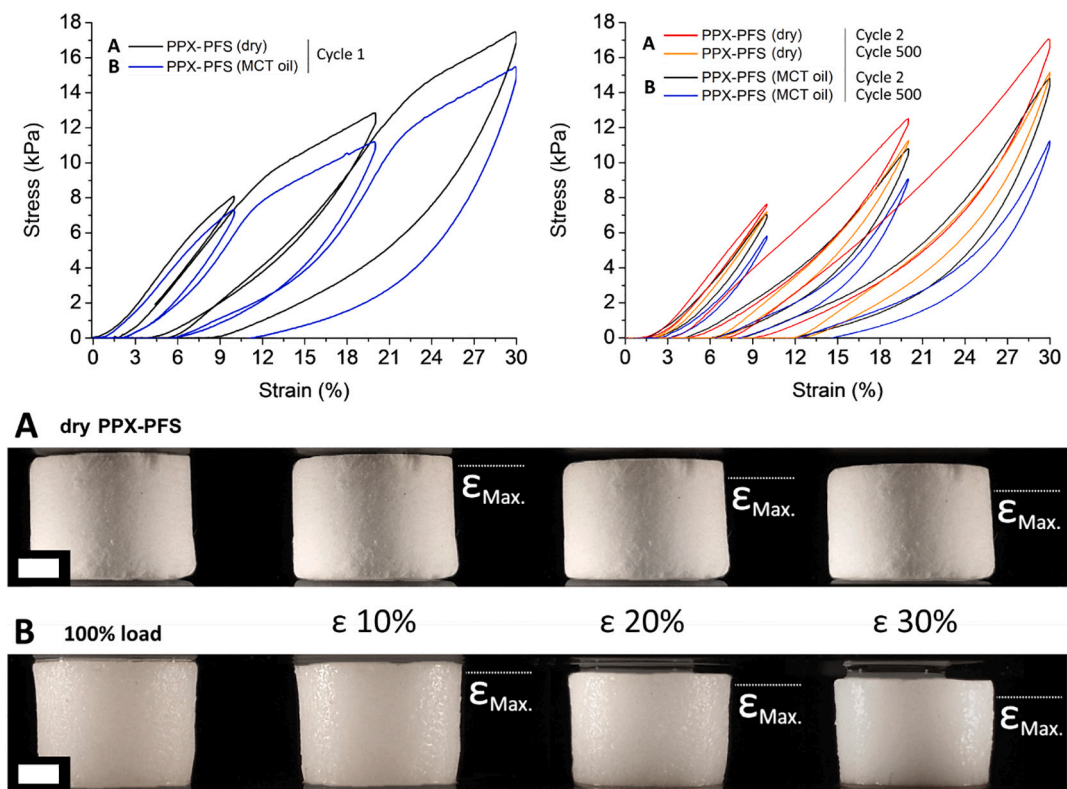
Fig. 4. Compression results for (top-left) the first and (top-right) the second as well as the 500th cycle of a compression sequence, shown section by section ranging from ε$_{Max.}$ 10% to 30%. (Bottom) PFS images prior and subsequently after each 500-cycle stage of the compression sequence, respectively. (Bar = 2 mm).
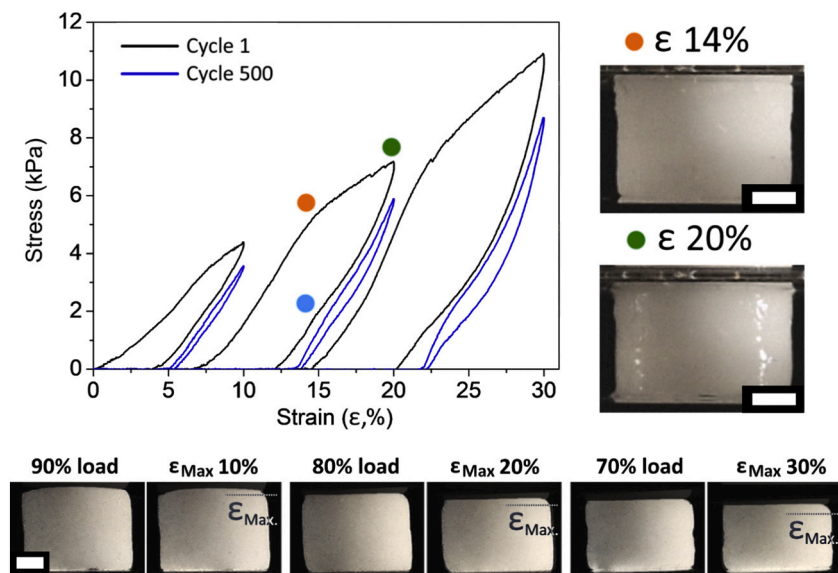

Fig. 5. Top: PFS compression results for a PFS loaded with (A) 90%, (B) 80% or (C) 70% MCT and compressed by ε$_{Max.}$ = (A) 10%, (B) 20% or (C) 30%. Bottom-row: PFS are shown for each load and corresponding ε$_{Max}$, in their initial state and after 500 cycles of compression, respectively. (Bar = 2 mm).

molecules immobilized at the surface of the PPX-coated fibers, undergoing surface-relaxation, spin-spin interaction between the oil and the PFS material. The size of the peak at 1 ms, about 30% of the integral, indicates that a considerable fraction of the MCT is interacting with the PPX surface, e.g., by van-der-Waals interactions, due to the large surface to volume ratio of the PFS scaffold.

The size and distribution of pores in PFS before coating is given in (Mader et al., 2018), showing a dual pore structure with diameters of 20–140 μm. The larger pores allow free diffusion of MCT and bulk-relaxation. In the smaller pores restriction of free diffusion could also affect T_2 values as MCT molecules are more likely to reach the matrix material and undergo surface-relaxation. A relation between smaller pore size and shorter T_2 is well established and utilized in different fields of research, such as geology and radiology (Davis et al., 1986; Fantazzini et al., 2003; Kleinberg, 1994; Kleinberg and Horsfield, 1990).
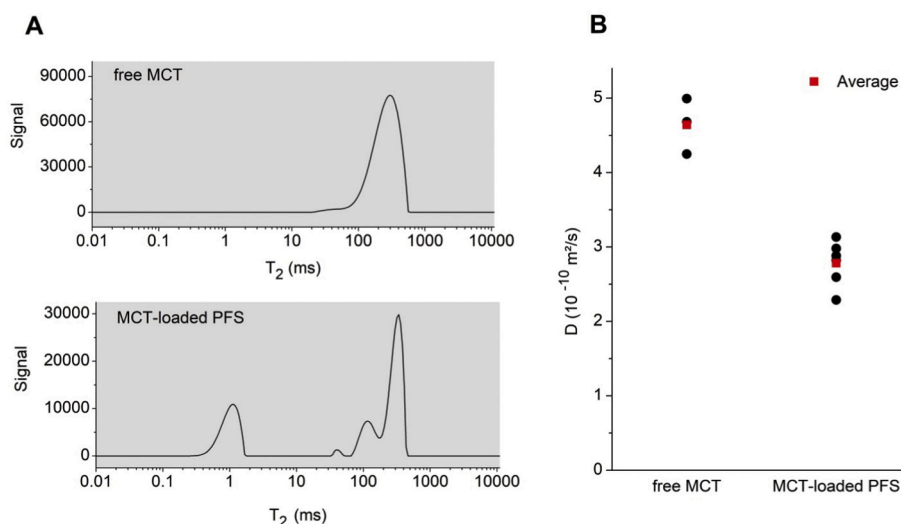
Fig. 6. ^{1}H NMR spectroscopy of free MCT and MCT-loaded PFS. **A:** exemplary T_2 distribution of free MCT (top) and MCT-loaded PFS (bottom) at 37 °C, **B:** Diffusion coefficient D at 37 °C of free MCT (triplicate, average $D = (4.6 \pm 0.4) \, 10^{-10} \, m^2/s$) and six PFS loaded with MCT (average $D = (2.8 \pm 0.3) \, 10^{-10} \, m^2/s$).

3.5.2. Diffusion coefficient D

Similar to the measurement of T_2, the diffusion coefficient D can also render information on the size of small structures, such as liquid-filled pores or emulsion droplets. If free movement of molecules is restricted, D decreases with pore or droplet size (Broekmann, 2002; Morgan et al., 2019). Molecules reaching a barrier are "bouncing off" and back in the opposite direction, their signal wrongly attributed to molecules that travel slower. D of free MCT and the oil immobilized in the PFS, likewise obtained with ^{1}H NMR, are given in Fig. 6 (right). D was slightly lower for the MCT-loaded PFS, confirming the restriction of diffusion in the scaffold. As only one value for D was acquired for each PFS, we cannot determine if there were different populations of D contributing to an overall reduction but, considering the T_2 results, it is highly possible. Also, measurement of D in a porous system is time depended because with increasing time more molecules reach the matrix and experience restriction. This is not depicted as we only obtained one value for D.

3.6. EPR drug-release studies

To evaluate whether drug release from oil loaded PFS is affected by the restricted diffusion in and interaction with the scaffold, we performed a simple release experiment. The release of dTempol, as a model-substance of a small-molecule drug, from free oil and MCT-soaked PFS was followed using standard EPR.

Considering the cylindrical shape of the PFS and oil (Fig. 7, left), we expect the diffusion of dTempol to the oil-PBS interface, a distance of up to 6 mm, to be the main mechanism governing the release process. The diffusion of the spin probe in MCT can be described using Fick's first law of diffusion (Fick, 1851), with J being the flux of dTempol, D the diffusion coefficient and $\frac{d\varphi}{dx}$ the concentration gradient.

$$J = -D \frac{d\varphi}{dx}$$

Dimensions and drug-loading of the immobilized and free MCT were equal. The area of the interface between oil and PBS was kept identical by our custom-made sample holders, and sink conditions in the receptor medium were assured. Hence the only variable expected to change the flux of the model drug to the oil-PBS interface is D. Drug release from the oil immobilized in the PFS was quite similar to the release from bulk MCT (Fig. 7, right). This can be explained with the high porosity and interconnectivity of the pore-system, which only slightly restricts the diffusion of small molecules within the PFS scaffold.

4. Conclusion

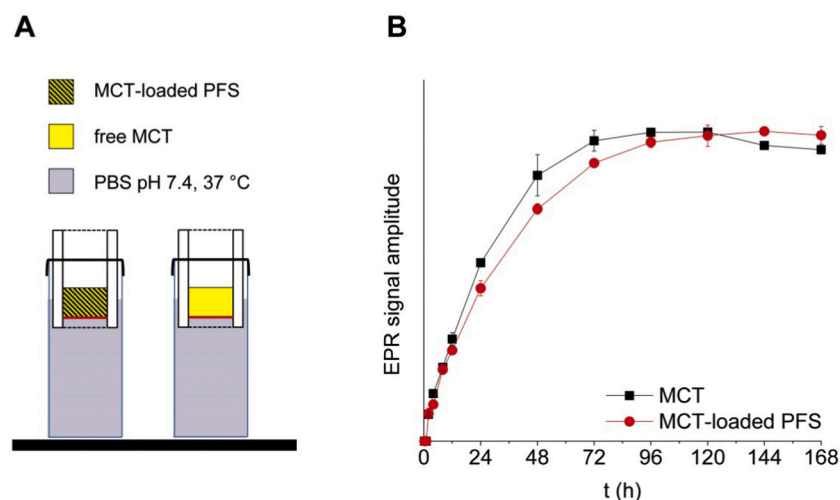Our experiments provide new insights into the physical processes

Fig. 7. Left) Setup for release study of dTempol from MCT. The red line indicates the interface between oil and PBS, kept at 50.3 mm^2 for both, free MCT and oil immobilized in the scaffolds. **Right)** Release of dTempol from free MCT and MCT-loaded PFS, given as signal amplitude of x-band EPR spectroscopy measurements. MCT is spiked with 10 mM dTempol; release was assayed in PBS pH 7.4 at 37 °C.

present within polymer fiber sponges. They further promote their applicability as multi-component drug delivery systems, for both, drug incorporation directly within the PFS scaffold as well as loading with drug-solutions after fabrication.

The different implantation model-scenarios and model-liquids tested reveal how the fluid-uptake and the prevailing scaffold interactions can be used to impact drug release from PFS. Noninvasive EPR and µCT imaging traced and quantified the progression of liquid-penetration. We identified the governing parameters to be considered in a typical application-scenario, mainly the wettability of the PFS but also the implantation site because liquid-infiltration rates are strongly influenced by air encapsulation. Our results indicate how to employ these processes in prolonged drug release in an aqueous environment and achieve a reproducible and continuous extraction of drug incorporated in the PFS scaffolds.

The PFS oil-retention, reversible elasticity and structural integrity under typical mechanical application-stress situations were quantified for complete as well as partial PFS liquid-loading. The PFS can retain most of its shape and elasticity in all dry and liquid-load scenarios independent from the applied liquid-load and compression stress scenario, respectively. The NMR results revealed how MCT, a possible drug-carrier-liquid, interacts with the PFS on a molecular level, indicating that both surface-relaxation and bulk-relaxation occur. Diffusion-coefficient measurements showed a restriction of diffusion for oil molecules within the PFS scaffold. Surprisingly, comparative drug-release studies from PFS and free-liquid reveal that neither liquid-surface interaction nor restrained diffusion substantially impacts drug release from PFS. We can conclude that PFS can effectively immobilize liquids inside their network and preserve drug-solutions in a predefined geometry.

In this work, we kept most of the PFS properties constant to grant comparability of our results. However, PFS can easily be manufactured from and combined with various excipients to create user-adjustable properties capable of facing almost any site-specific requirements in the future. Based on the presented results, we want to elaborate the versatile tunability of PFS further to create mature multi-component drug-release platforms for pharmaceutical as well as tissue engineering applications.

Declaration of Competing Interest

The authors declare that they have no known competing financial interests or personal relationships that could have appeared to influence the work reported in this paper.

Acknowledgments

Appendix A. Supplementary data

Supplementary data to this article can be found online at https://doi.org/10.1016/j.ijpx.2020.100055.

References

Bagheri, A.R., Agarwal, S., Golenser, J., Greiner, A., 2017. Unlocking Nanocarriers for the Programmed Release of Antimalarial Drugs. Glob. Challenges 1, 1600011. https://doi.org/10.1002/gch2.201600011.

Broekmann, I., 2002. PFG-NMR-Untersuchungen an Monoglycerid-Gelen Und Wasser-in-Öl-Emulsionen (Doctoral Dissertation).

Davis, C.A., Genant, H.K., Dunham, J.S., 1986. The Effects of Bone on Proton NMR Relaxation Tiimes of Surrounding Liquids.

Duan, G., Jiang, S., Jérôme, V., Wendorff, J.H., Fathi, A., Uhm, J., Altstädt, V., Herling, M., Breu, J., Freitag, R., Agarwal, S., Greiner, A., 2015. Ultralight, soft polymer sponges by self-assembly of short electrospun fibers in colloidal dispersions. Adv. Funct. Mater. 25, 2850–2856. https://doi.org/10.1002/adfm.201500001.

Duan, G., Jiang, S., Moss, T., Agarwal, S., Greiner, A., 2016. Ultralight open cell polymer sponges with advanced properties by PPX CVD coating. Polym. Chem. 7, 2759–2764. https://doi.org/10.1039/c6py00339g.

Duan, G., Bagheri, A.R., Jiang, S., Golenser, J., Agarwal, S., Greiner, A., 2017a. Exploration of Macroporous Polymeric Sponges as Drug Carriers. Biomacromolecules 18, 3215–3221. https://doi.org/10.1021/acs.biomac.7b00852.

Duan, G., Koehn-Serrano, M., Greiner, A., 2017b. Highly Efficient Reusable Sponge-Type Catalyst Carriers based on Short Electrospun Fibers. Macromol. Rapid Commun. 38, 1–6. https://doi.org/10.1002/marc.201600511.

Duarte, A., Patricio, J., Pereira, A., Gil, M., Cabrita, A., Barros, M., Cartucho, D., 2005. Immobilisation of Cardosin A in Chitosan Sponges as a Novel Implant for Drug delivery. Curr. Drug Discov. Technol. 2, 231–238. https://doi.org/10.2174/157016305775202973.

Fantazzini, P., Brown, R.J.S., Borgia, G.C., 2003. Bone tissue and porous media: Common features and differences studied by NMR relaxation. Magn. Reson. Imaging 21, 227–234. https://doi.org/10.1016/S0730-725X(03)00129-2.

Fick, A., 1851. Über Diffusion. Ann. Phys. 170, 59–86.

Greiner, A., Wendorff, J.H., 2007. Electrospinning: a fascinating method for the preparation of ultrathin fibers. Angew. Chemie - Int. Ed. 46, 5670–5703. https://doi.org/10.1002/anie.200604646.

Guo, N., Zhang, Q., Sun, Y., Yang, H., 2019. Separation and identification of acylated leuprorelin inside PLGA microspheres. Int. J. Pharm. 560, 273–281. https://doi.org/10.1016/j.ijpharm.2019.01.061.

Jennings, J.A., Beenken, K.E., Parker, A.C., Smith, J.K., Courtney, H.S., Smeltzer, M.S., Haggard, W.O., 2016. Polymicrobial Biofilm Inhibition Effects of Acetate-Buffered Chitosan Sponge delivery device. Macromol. Biosci. 16, 591–598. https://doi.org/10.1002/mabi.201500347.

Jiang, S., Chen, Y., Duan, G., Mei, C., Greiner, A., Agarwal, S., 2018. Electrospun nanofiber reinforced composites: a review. Polym. Chem. 9, 2685–2720. https://doi.org/10.1039/c8py00378e.

Kassem, M.A.A., ElMeshad, A.N., Fares, A.R., 2015. Lyophilized Sustained Release Mucoadhesive Chitosan Sponges for Buccal Buspirone Hydrochloride delivery: Formulation and in Vitro Evaluation. AAPS PharmSciTech 16, 537–547. https://doi.org/10.1208/s12249-014-0243-3.

Kempe, S., Metz, H., Mäder, K., 2010. Application of Electron Paramagnetic Resonance (EPR) spectroscopy and imaging in drug delivery research - Chances and challenges. Eur. J. Pharm. Biopharm. 74, 55–66. https://doi.org/10.1016/j.ejpb.2009.08.007.

Kleinberg, R.L., 1994. Pore size distributions, pore coupling, and transverse relaxation spectra of porous rocks. Magn. Reson. Imaging 12, 271–274. https://doi.org/10.1016/0730-725X(94)91534-2.

Kleinberg, R.L., Horsfield, M.A., 1990. Transverse relaxation processes in porous sedimentary rock. J. Magn. Reson. 88, 9–19. https://doi.org/10.1016/0022-2364(90)90104-H.

Li, J., Xu, W., Li, D., Liu, T., Zhang, Y.S., Ding, J., Chen, X., 2018. Locally Deployable Nanofiber Patch for Sequential Drug delivery in Treatment of primary and Advanced Orthotopic Hepatomas. ACS Nano 12, 6685–6699. https://doi.org/10.1021/acsnano.8b01729.

Lucke, A., Kiermaier, J., Göpferich, A., 2002. Peptide Acylation by Poly(α-Hydroxy Esters). Pharm. Res. 19, 175–181. https://doi.org/10.1023/A:1014272816454.

Lurie, D.J.D.J., Mäder, K., 2005. Monitoring drug delivery processes by EPR and related techniques - Principles and applications. Adv. Drug Deliv. Rev. 57, 1171–1190. https://doi.org/10.1016/j.addr.2005.01.023.

Mäder, K., Gallez, B., Liu, K.J., Swartz, H.M., 1996. Non-invasive in vivo characterization of release processes in biodegradable polymers by low-frequency electron paramagnetic resonance spectroscopy. Biomaterials 17, 457–461. https://doi.org/10.1016/0142-9612(96)89664-5.

Mäder, K., Bacic, G., Domb, A., Elmalak, O., Langer, R., Swartz, H.M., 1997. Noninvasive in Vivo monitoring of Drug Release and Polymer Erosion from Biodegradable Polymers by EPR Spectroscopy and NMR Imaging. J. Pharm. Sci. 86, 126–134. https://doi.org/10.1021/js9505105.

Mader, M., Jérôme, V., Freitag, R., Agarwal, S., Greiner, A., 2018. Ultraporous, Compressible, Wettable Polylactide/Polycaprolactone Sponges for Tissue Engineering. Biomacromolecules 19, 1663–1673. https://doi.org/10.1021/acs.biomac.8b00434.

Miszuk, J.M., Xu, T., Yao, Q., Fang, F., Childs, J.D., Hong, Z., Tao, J., Fong, H., Sun, H., 2018. Functionalization of PCL-3D electrospun nanofibrous scaffolds for improved BMP2-induced bone formation. Appl. Mater. Today 10, 194–202. https://doi.org/10.1016/j.apmt.2017.12.004.

Morgan, V., Sad, C., Constantino, A., Azeredo, R., Lacerda, V., Castro, E., Barbosa, L., 2019. Droplet Size Distribution in Water-Crude Oil Emulsions by Low-Field NMR. J. Braz. Chem. Soc 30, 1587–1598. https://doi.org/10.21577/0103-5053.20190057.

Parker, A.C., Beenken, K.E., Jennings, J.A., Hittle, L., Shirtliff, M.E., Bumgardner, J.D., Smeltzer, M.S., Haggard, W.O., 2015. Characterization of local delivery with amphotericin B and vancomycin from modified chitosan sponges and functional biofilm prevention evaluation. J. Orthop. Res. 33, 439–447. https://doi.org/10.1002/jor.22760.

Ranganath, S.H., Wang, C.H., 2008. Biodegradable microfiber implants delivering paclitaxel for post-surgical chemotherapy against malignant glioma. Biomaterials 29, 2996–3003. https://doi.org/10.1016/j.biomaterials.2008.04.002.

Schädlich, A., Kempe, S., Mäder, K., 2014. Non-invasive in vivo characterization of microclimate pH inside in situ forming PLGA implants using multispectral fluorescence imaging. J. Control. Release 179, 52–62. https://doi.org/10.1016/j.jconrel.2014.01.024.

Schreier, B., Rabe, S., Winter, S., Ruhs, S., Mildenberger, S., Schneider, B., Sibilia, M.,

Gotthardt, M., Kempe, S., Mäder, K., Grossmann, C., Gekle, M., 2014. Moderate in-appropriately high aldosterone/NaCl constellation in mice: Cardiovascular effects and the role of cardiovascular epidermal growth factor receptor. Sci. Rep. 4. https://doi.org/10.1038/srep07430.

Si, Y., Yu, J., Tang, X., Ge, J., Ding, B., 2014. Ultralight nanofibre-assembled cellular aerogels with superelasticity and multifunctionality. Nat. Commun. 5. https://doi.org/10.1038/ncomms6802.

Si, Y., Fu, Q., Wang, X., Zhu, J., Yu, J., Sun, G., Ding, B., 2015. Superelastic and Superhydrophobic Nanofiber-Assembled Cellular Aerogels for Effective Separation of Oil/Water Emulsions. ACS Nano 9, 3791–3799. https://doi.org/10.1021/nn506633b.

Si, Y., Wang, X., Dou, L., Yu, J., Ding, B., 2018. Ultralight and fire-resistant ceramic nanofibrous aerogels with temperature-invariant superelasticity. Sci. Adv. 4. https://doi.org/10.1126/sciadv.aas8925.

Siepmann, J., Elkharraz, K., Siepmann, F., Klose, D., 2005. How autocatalysis accelerates drug release from PLGA-based microparticles: a quantitative treatment. Biomacromolecules 6, 2312–2319. https://doi.org/10.1021/bm050228k.

Simon, P., Mang, S., Hasenhindl, A., Gronski, W., Greiner, A., 1998. Poly(p-xylylene) and its derivatives by chemical vapor deposition: Synthesis, mechanism, and structure. Macromolecules 31, 8775–8780. https://doi.org/10.1021/ma9808070.

Tihan, G.T., Ungureanu, C., Barbaresso, R.C., Zgârian, R.G., Rau, I., Meghea, A., Albu, M.G., Ghica, M.V., 2015. Chloramphenicol collagen sponges for local drug delivery in dentistry. Comptes Rendus Chim. 18, 986–992. https://doi.org/10.1016/j.crci.2015.06.004.

Tseng, Y.Y., Wang, Y.C., Su, C.H., Liu, S.J., 2015. Biodegradable vancomycin-eluting poly [(d,l)-lactide-co-glycolide] nanofibres for the treatment of postoperative central nervous system infection. Sci. Rep. 5, 1–7. https://doi.org/10.1038/srep07849.

Washburn, E.W., 1921. Note on the dynamics of capillary flow. Phys. Rev. 17, 273–283. https://doi.org/10.1103/PhysRev.18.206.

Yohe, S.T., Colson, Y.L., Grinstaff, M.W., 2012. Superhydrophobic materials for tunable drug release: using displacement of air to control delivery rates. J. Am. Chem. Soc. 134, 2016–2019. https://doi.org/10.1021/ja211148a.

Yu, H., Chen, X., Cai, J., Ye, D., Wu, Y., Fan, L., Liu, P., 2019. Novel porous three-dimensional nanofibrous scaffolds for accelerating wound healing. Chem. Eng. J. 369, 253–262. https://doi.org/10.1016/j.cej.2019.03.091.

Zhang, Z., Kuang, G., Zong, S., Liu, S., Xiao, H., Chen, X., Zhou, D., Huang, Y., 2018. Sandwich-like Fibers/Sponge Composite Combining Chemotherapy and Hemostasis for Efficient Postoperative Prevention of Tumor Recurrence and Metastasis. Adv. Mater. 30, 1–9. https://doi.org/10.1002/adma.201803217.